PROCEEDINGS OF SPIE

SPIEDigitalLibrary.org/conference-proceedings-of-spie

Robust x-ray based material identification using multi-energy sinogram decomposition

Yaoshen Yuan
Brian Tracey
Eric Miller

SPIE.

Robust X-ray based material identification using multi-energy sinogram decomposition

Yaoshen Yuan[a], Brian Tracey[b], and Eric Miller[c]

[abc]ECE department, Tufts University, 161 College Ave, Medford, MA 02155 US

ABSTRACT

There is growing interest in developing X-ray computed tomography (CT) imaging systems with improved ability to discriminate material types, going beyond the attenuation imaging provided by most current systems. Dual-energy CT (DECT) systems can partially address this problem by estimating Compton and photoelectric (PE) coefficients of the materials being imaged, but DECT is greatly degraded by the presence of metal or other materials with high attenuation. Here we explore the advantages of multi-energy CT (MECT) systems based on photon-counting detectors. The utility of MECT has been demonstrated in medical applications where photon-counting detectors allow for the resolution of absorption K-edges. Our primary concern is aviation security applications where K-edges are rare. We simulate phantoms with differing amounts of metal (high, medium and low attenuation), both for switched-source DECT and for MECT systems, and include a realistic model of detector energy 0resolution. We extend the DECT sinogram decomposition method of Ying *et al.* to MECT, allowing estimation of separate Compton and photoelectric sinograms. We furthermore introduce a weighting based on a quadratic approximation to the Poisson likelihood function that deemphasizes energy bins with low signal. Simulation results show that the proposed approach succeeds in estimating material properties even in high-attenuation scenarios where the DECT method fails, improving the signal to noise ratio of reconstructions by over 20 dB for the high-attenuation phantom. Our work demonstrates the potential of using photon counting detectors for stably recovering material properties even when high attenuation is present, thus enabling the development of improved scanning systems.

Keywords: Computed tomography, multi-energy bins, high attenuation, Compton and photoelectric reconstructions

1. INTRODUCTION

X-ray Computed tomography (CT) has been widely used in explosive detection. Especially in aviation security, CT scanning plays an important role because of its maturity as well as safety.[1,2] Traditionally, monoenergetic CT is used to estimate the attenuation of object, based on data from detectors that integrate over the entire energy spectrum. However, material discrimination in monoenergetic systems suffers as only a single physical parameter can be estimated. With dual-energy scanners, it is possible to estimate both density and the effective atomic number Z_{eff}, which can be employed to categorize different materials.[3,4] Several techniques for acquiring dual energy X-ray data have been developed, including switching the source spectrum or inserting layered filters in front of detectors to give low- and high-energy readouts.[1] Because attenuation can be expressed as the sum of Compton and photoelectric (PE) coefficients with respect to energy, Compton and PE coefficients can be used to effectively identify different materials.[5] Ying *et al* have proposed an approach for estimating Compton and PE coefficients from dual-energy CT (DECT) data.[6]

For both monoenergetic and dual-energy systems, the presence of material with high attenuation such as metal can severely corrupt reconstructed images, producing artifacts such as streaks and cupping that negatively influences object identification.[7,8] This degradation reflects the fact that photon counts received by detectors

Further author information: (Send correspondence to Yaoshen Yuan)
Yaoshen Yuan: E-mail: yaoshen.yuan@tufts.edu, Telephone: 1 781 827 1376
Brian Tracey: E-mail: btracey@eecs.tufts.edu, Telephone: 1 617 627 6424
Eric Miller: E-mail: elmiller@ece.tufts.edu, Telephone: 1 617 627 0835

Anomaly Detection and Imaging with X-Rays (ADIX), edited by
Amit Ashok, Mark A. Neifeld, Michael E. Gehm, Proc. of SPIE Vol. 9847,
98470V · © 2016 SPIE · CCC code: 0277-786X/16/$18 · doi: 10.1117/12.2222584

are greatly reduced by highly attenuating materials, so the sinogram is degraded.[9] For the decomposition of dual-energy sinograms into Compton and PE sinograms, metal can also cause severe artifacts.

Recently, multi-energy detectors have been developed that are capable of discriminating up to 256 energy bins by photon counting. Results have been presented arguing that these detectors provide more accurate material property estimates than dual energy X-ray.[10] In our paper, we will present an new weighted least squares approach to decomposing sinograms into Compton and PE, using multi-energy data from photon counting detectors. We will demonstrate that this approach reduces the artifacts caused by metal.

The paper is constructed in the following way. In the Methods section, we will introduce the basic model as well as the method we used to reconstruct Compton and PE images. In Numerical Studies, we will describe the phantoms used in our simulations and the source, detectors and noise. The model of realistic energy resolution will also be described in this section. In Results, the reconstructed images and data analysis will be presented. Finally, the Conclusions section contains a summary of the work.

2. METHODS

2.1 Sinogram Decomposition

There are two factors that contribute to the X-ray attenuation in the energy range of interest. One is the Compton scattering, and another is the photoelectric effect.[5] The use of these two effects can help distinguish different materials because of their specific scattering and photoelectric properties. The attenuation coefficient $\mu(E)$ can then be represented by a linear combination of Compton a_c and photoelectric coefficient a_p. The relationship between attenuation and Compton as well as photoelectric coefficients is defined as:[11]

$$\mu(x,y;E) = a_c(x,y)f_{KN}(E) + a_p(x,y)f_p(E) \tag{1}$$

where (x,y) represents the coordinates and E stands for the incident energy. Function $f_p(E)$ and $f_{KN}(E)$ are called basis functions, which is related to the energy. $f_p(E)$ approximates the energy dependence of the photoelectric interaction, which is defined as:

$$f_p(E) = E^{-3}. \tag{2}$$

$f_{KN}(E)$ is the Klein-Nishina function, meaning the energy dependence of total cross section for Compton scattering. It can be described as follows:[5]

$$f_{KN}(\alpha) = \frac{1+\alpha}{\alpha^2}\left[\frac{2(1+\alpha)}{1+2\alpha} - \frac{1}{\alpha}\ln(1+2\alpha)\right] + \frac{1}{2\alpha}\ln(1+2\alpha) - \frac{(1+3\alpha)}{(1+2\alpha)^2}. \tag{3}$$

The measured data at each energy depends on the line integral along each raypath, i.e. $\int_{S_i}\mu(x,y;E)dl$ where S_i is the raypath for the ith ray. Substituting in from Eq. 1, we can define a linear relation

$$\int_{S_i}\mu(x,y;E)dl = A_c^i f_{KN}(E) + A_p^i f_p(E) \tag{4}$$

where for the ith ray,

$$A_c^i = \int_{S_i} a_c(x,y)dl \qquad \text{and} \qquad A_p^i = \int_{S_i} a_p(x,y)dl \tag{5}$$

Thus the equations above convert a_c and a_p to the projection form A_c and A_p, where A_c and A_p are the line integrals of a_c and a_p.

Because of the linear relation described above (Eq.4), we can recover A_c and A_p from the projection of attenuation. Here we build on Ying's method to decompose the dual energy as well as multiple energy projections into Compton and photoelectric projections.[6] The reconstruction of A_c and A_p can be transferred to a constrained minimization problem, which finds the solution, A_c and A_p, to minimize the least square error between the

measured projections and modeled projections. Here we define $\theta^i = [A_c^i, A_p^i]$. Thus for dual energy decomposition problem, the minimization of least square error can be described as:

$$\theta^i = \arg\min_{\theta^i} [K_L(\theta^i) - m_L^i]^2 + [K_H(\theta^i) - m_H^i]^2 \tag{6}$$

with the constraints:

$A_c^i \geq 0 \quad \text{and} \quad A_p^i \geq 0$

where m_L^i and m_H^i represent the log-normalized measured projections along the ith path for low and high energy spectra respectively. $K_L(\theta^i)$ and $K_H(\theta^i)$ denote the log-normalized modeled projection derived from the linear relationship between μ and A_c, A_p (Eq.4), which are:

$$K_l(\theta^i) = -\ln\left[\int S_l(E) exp(-A_c^i f_{KN}(E) - A_p^i f_p(E)) dE\right] + \ln \int S_l(E) dE \tag{7}$$

where l represents lth energy bin. Therefore, Eq.6 shows we seek A_c and A_p that minimizes this cost function.

By using least square error, we can generalize Eq.6 to the multi-energy situation. Unlike the dual energy case, the multi-energy case has more than two terms in the cost function that needs to be minimized because the spectrum is separated into multiple bins. Thus for multiple energies, the least squares minimization problem is:

$$\theta^i = \arg\min_{\theta^i} \sum_{l=1}^{M} [K_l(\theta^i) - m_l^i]^2 \tag{8}$$

where m_l^i represents the log-normalized measured projection along ith ray for lth energy bin and $K_l(\theta^i)$ is the log-normalized modeled projection for lth bin given θ^i. M denotes the number of energy bins.

To acquire θ^i that minimizes the cost function, multivariate Newton-Raphson theory can be used.

2.2 Weighted Sinogram Decomposition

Eq.8 shows that we can obtain Compton and photoelectric images by minimizing least square error. However, for each bin, the uncertainty increases with the decrease of number of photons measured, especially for the low-energy bins, which can be affected more strongly by metal or other highly attenuating materials. Therefore, in order to get better approximations for A_c and A_p, weighted least square error can be employed.

Bouman and Sauer give the quadratic approximation of the Poisson log-likelihood function for X-ray transmission problem using a Taylor series expansion, which can be described as:[12–14]

$$logP(\boldsymbol{M} = \boldsymbol{m^i}|\theta^i) \approx -\frac{1}{2}(\boldsymbol{K}(\theta^i) - \boldsymbol{m^i})^T \boldsymbol{\Sigma} (\boldsymbol{K}(\theta^i) - \boldsymbol{m^i}) + \boldsymbol{c}(\theta^i) \tag{9}$$

where $\boldsymbol{\Sigma}$=diag$\{\boldsymbol{w}\}$ and $\boldsymbol{w}$ is the number of photon counts received in each energy bin. Vector $\boldsymbol{K}(\theta^i)$ is the M dimensional column vector of log-normalized mean values determined by θ^i=$[A_c^i, A_p^i]$ for different bins while $\boldsymbol{m^i}$ is the M dimensional column vector of log-normalized measured projections. Therefore, here we generalize the weighting method given by Bouman and Sauer to minimize the error term for each energy bin. (Eq.10).

$$(\theta^i) = \arg\min_{\theta^i} (\boldsymbol{K(\theta^i)} - \boldsymbol{m^i})^T \boldsymbol{\Sigma} (\boldsymbol{K(\theta^i)} - \boldsymbol{m^i}) \tag{10}$$

In order to make it comparable to Eq.8, it can also be written as following expansion:

$$\theta^i = \arg\min_{\theta^i} \sum_{l=1}^{M} w_l^i [K_l(\theta^i) - m_l^i]^2 \tag{11}$$

where w_l^i is the number of photon counts detected at lth bin for the ith ray.

This weighting matrix $\boldsymbol{\Sigma}$ gives more weight to the raypaths and energy bins whose measured photon count is larger. For rays passing through metal objects, this gives more weighting to the high energy bins.

Table 1. Both low and high energy source spectra are used for the realistic dual-energy simulation. Only a single high energy spectrum is used for other cases. Here we assume integrating detector is implemented for realistic dual-energy CT and photon counting detector with a varying number of energy bins is used for other simulations.

Case	Detector type	Spectra used	# of bins
Switched dual-energy (SwDE)	integrating	low and high energy spectra from left one of Fig. 3	N/A
Ideal dual-energy (IdDE)	photon counting (no overlap)	high energy spectrum from left one of Fig. 3	2
Ideal 7 bin	photon counting (no overlap)	high energy spectrum	7
Realistic 7 bin	photon counting (realistic overlap)	high energy spectrum	7

3. NUMERICAL STUDIES

3.1 Description of the numerical experiments

3.1.1 Phantoms

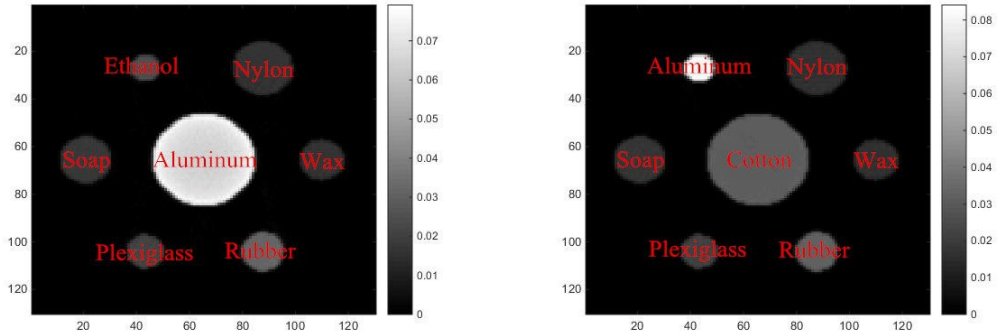

Figure 1. Left one indicates the phantom with high attenuation. Right one presents the phantom with medium attenuation. Phantom with low attenuation has the same geometry as that with high attenuation but aluminum is replaced by cotton.

In this work, three different types of phantoms were used for simulation to explore how the amount of metal affects the accuracy of Compton and photoelectric (PE) reconstruction. First, we used a phantom (left figure of Fig. 1, called "high attenuation"), which includes aluminum, soap, ethanol, nylon, wax, rubber and plexiglass. This simulates the situation where a large amount of metal is in the phantom. The second phantom ("medium attenuation") has the same geometry but the middle circle is replaced by cotton and the small circle of ethanol is replaced by aluminum (right figure of Fig. 1, which represents the situation where a small amount of metal is present. In the third phantom ("low attenuation"), the aluminum circle in the first phantom is replaced by cotton to simulate the situation where there is no metal.

3.1.2 Sources

A variety of source spectra and detectors are used, as summarized in Table 1. The left column shows the source spectra utilized. In simulation and subsequent processing, we used the spectra from the paper of Semerci and Miller.[15] The spectra consist of two individual spectra, a low-energy spectrum and a high-energy spectrum. The low-energy spectrum spans from 8 keV to 80 keV and the high-energy spectrum spans from 14 keV to 139 keV (Fig. 3). The high- and low-energy spectra are used to model switched dual energy CT (abbreviated 'SwDE'), in which source voltage is switched electronically and the object is scanned twice. The integrating detector will then measure the photons for each of the spectra.

For other simulations, we used only a single spectrum, the high-energy scan from Fig. 3. In these simulations, we assume the detector can discriminate photon energy. For multi-energy (ME) simulations, we divide the

spectrum into multiple evenly-spaced bins (7, 128, etc) to simulate photon-counting detectors. As a special case, we consider the case of 2 ideal bins, and call this 'ideal dual-energy', or 'IdDE'. In addition to ideal bins, we also examine the effects of realistic energy resolution in detectors, as described below. The detailed description will be given in the next section.

Intuitively, it may be unclear how to compare SwDE and IdDE. However, the results show that IdDE performance is better than SwDE, even though IdDE only uses one scan while the SwDE is able to use a second scan, which provides more information about the phantom. This performance improvement shows the promise of photon-counting detectors.

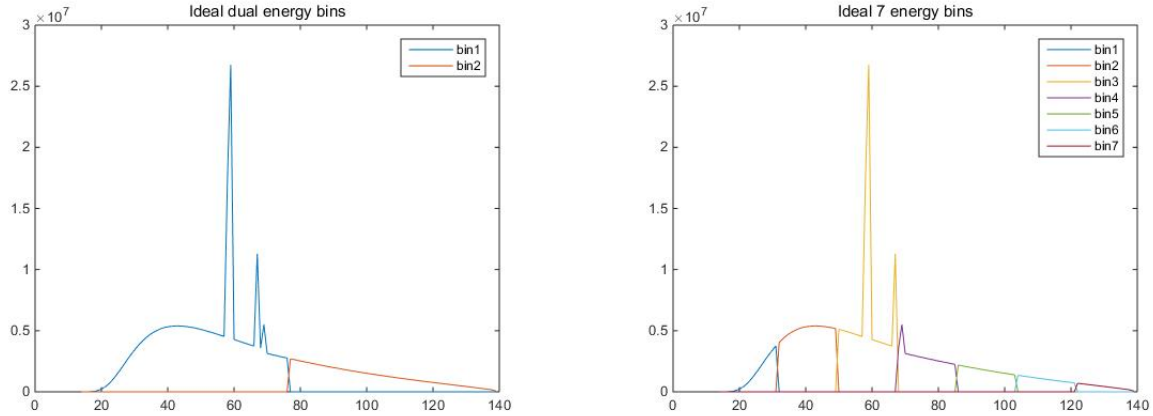

Figure 2. The figure shows the ideal case where the detected spectra can be ideally split into multiple bins for the ideal case. The left plot is the dual-energy spectrum and the right one is the multi-energy spectrum (7 bins).

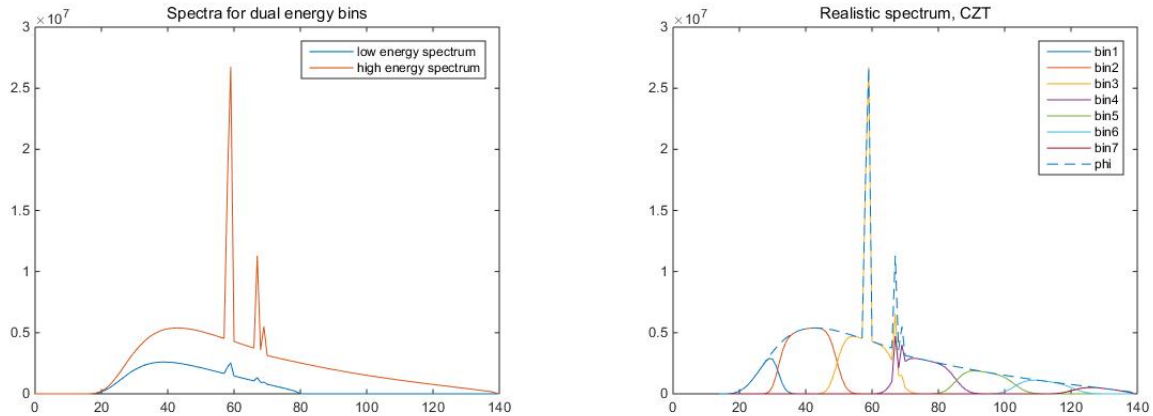

Figure 3. Realistic simulation cases. The left plot shows two independent source spectra for realistic dual-energy case (SwDE). The right plot shows a realistic photon counting detector splits the high energy spectrum (only high energy spectrum was used) into 7 bins imperfectly because of the finite energy resolution.

3.1.3 Detectors

There are two different types of detectors used in the computed tomography (CT), namely integrating detectors and photon counting detectors. An integrating detector converts the electrical charge into the number of photons by amplification and digitalization. Integrating detectors do not give information about the energy of the detected photons. A photon counting detector transfers the photon into electrical pulse. The energy of the photon determines the amplitude of electrical pulse, by which the number of photons at specific energy bin can be determined.[11,15,16] For our studies of SwDE, an integrating detector was simulated so both Poisson and

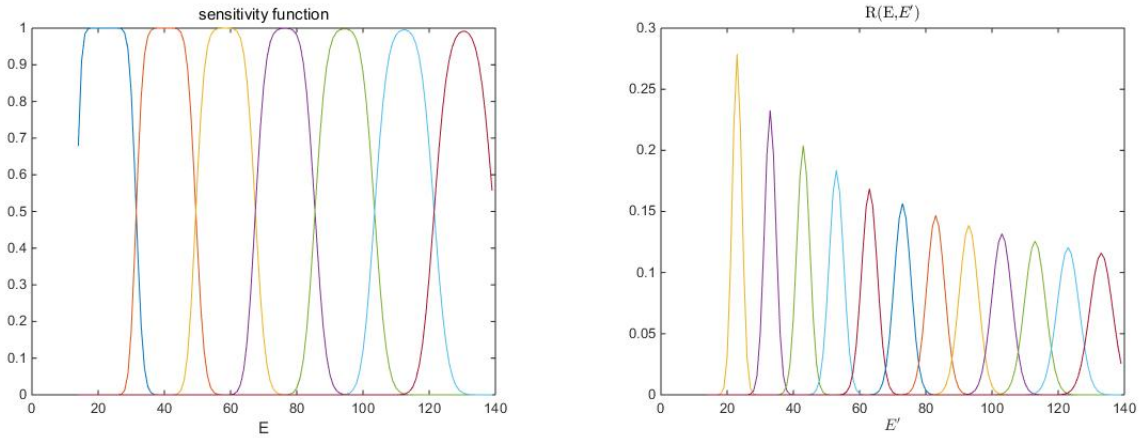

Figure 4. Sensitivity function determines the received spectrum for each bins and Gaussian response function describes the probability of the detected photon energy, which also determines the sensitivity function.

Gaussian noise (SNR=60 dB) were added to the number of photons detected (for details, see [11]) For multi-energy studies, a photon counting detector was assumed, where readout noise is eliminated. Thus only Poisson noise was added in the simulation.

We simulated both ideal and realistic multi-energy detectors. For the ideal situation, we assume that the detector can perfectly divide the spectrum into bins, with no overlap between two consecutive bins. For instance, for the ideal 7 bins simulation, which was used in this paper, the spectrum will be evenly divided into 14 to 31 keV, 32 to 49 keV, ..., 127 to 139 keV (Fig. 2).However, realistic multi-energy detectors do not have perfect energy resolution. The model from Roessl and Herrmann[17] gives a realistic model for the resolution of photon counting detectors. A sensitivity function is added to the model to produce the overlapped spectrum (right figure of Fig. 3). In Fig. 4, sensitivity function as well as Gaussian response function are shown given that Fano factor is 0.089 for sensor material CZT.

This model describes the finite energy resolution as follows:

$$\bar{\boldsymbol{Y}}_{\boldsymbol{l}} = \int_0^\infty S(E)\Omega_l(E)exp(-f_{KN}(E)\boldsymbol{A_c} - f_p(E)\boldsymbol{A_p})dE \tag{12}$$

where $\bar{\boldsymbol{Y}}_{\boldsymbol{l}}$ is the mean of Poisson random variable for the ith energy bin and $\Omega_i(E)$ is the sensitivity function for the ith energy bin. A photon with energy E can produce a signal with energy $E^{'}$. This can occur, for example, when two photons arrive nearly simultaneously, so the detector will detect the single photon with higher energy. In addition, the detector electronics are not perfectly able to measure photon energy. A sensitivity function (Eq.13) is therefore introduced which models the detected energy of a photon as a Gaussian distribution whose mean is the true energy of the photon.

$$R(E, E^{'}) = \frac{1}{\sqrt{2\pi}\sigma_E} e^{-\frac{(E^{'}-E)^2}{2\sigma_E^2}} \tag{13}$$

where $\sigma_E = k\sqrt{E}$. Here $k = \sqrt{fano}$, where $fano$ is the Fano factor of the sensor material. Therefore, in order to simulate the spectrum for each energy bin, a Gaussian spectral response $R(E, E^{'})$ corresponding to each energy E should be integrated within the range of the energy bin. This integration is the sensitivity function,

$$\Omega_l(E) = \int_{E_l}^{E_{l+1}} R(E, E^{'})dE^{'} \tag{14}$$

where $\Omega_l(E)$ is the sensitivity function for lth bin. By multiplying the sensitivity function with the source spectrum, the spectrum for each bin can be obtained and used in Eq.12.

Table 2. PSNR for different sceneries. Left sub-column is PSNR for Compton reconstruction and right sub-column is for PE reconstruction. 'Mismatch' means using ideally divided multi-bins spectrum to recover Compton and PE and 'match' means using realistic spectrum which is identical to the spectrum used to build the sinograms to reconstruct.

	SwDE (poi+gau)		**ideal DE** (poi+gau)		**real 7 bin** (poi,match)		**ideal 7 bin** (poi)		**real 7 bin** (mismatch)	
High, no weight	14.35	14.22	27.59	24.73	51.57	47.02	48.01	43.52	35.17	30.62
High, weighting	33.30	28.53	45.78	35.40	74.70	71.08	74.60	71.28	49.80	49.05
Medium, no weight	27.56	29.18	31.47	29.20	65.20	71.45	74.05	77.41	49.49	46.62
Medium, weighting	45.19	47.44	54.58	53.47	80.23	84.72	80.21	84.53	53.75	53.83
Low, no weight	46.50	50.86	55.12	55.67	64.42	71.42	78.66	85.21	59.06	60.13
Low, weighting	46.52	50.90	55.12	55.71	80.66	86.75	80.87	87.06	60.13	62.54

3.2 Reconstruction and Metrics

For all phantoms, we simulated data acquisition at 180 angles (1 degree spacing) using the built-in Matlab 'radon' command. A separate simulation was done for each energy bin. Simulated dual- or multi-energy data were then decomposed into Compton and photoelectric sinograms using the weighted least squares method described above, and 'iradon' was used to reconstruct images of Compton and photoelectric coefficents.

To evaluate the accuracy of these images, peak signal to noise ratio (PSNR) was used. When computing PSNR, a peak value must be defined. Because the peak signal for these three phantom is generated by aluminum, we used the Compton and PE coefficients of aluminum as the peak signal level. The minimum square error (MSE) was also selected as the metric evaluating the reconstruction results. In section 4.2, we study the MSE of a specific region in the phantom, such as aluminum region, and its influence on the PSNR of the whole phantom.

In section 4.2, the relation between the number of energy bins and their corresponding mean square error (MSE) will be explored for various phantoms, to demonstrate how the number of energy bins influences the reconstructed results. In order to reduce the variance of samples, 30 random sinogram realizations (with random noise and Poisson statistics) were generated. MSEs for both Compton and PE images derived from each sample were then computed and the average MSE across all realizations was calculated.

4. RESULTS

4.1 Comparison between SwDE and Weighted MECT

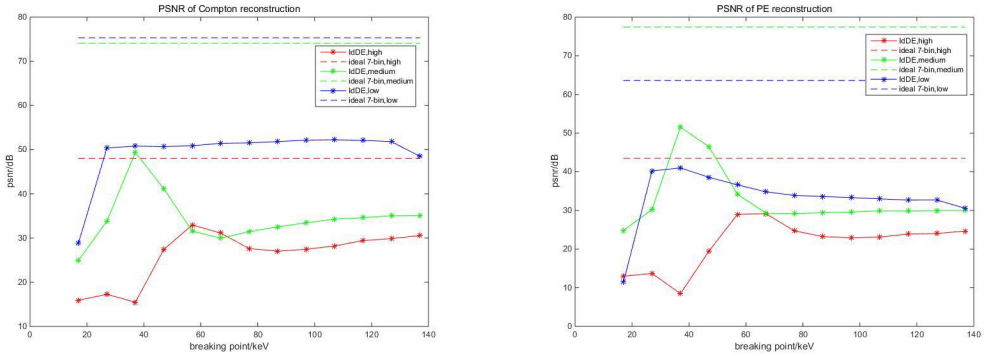

Figure 5. The plots show the PSNR of non-weighting Compton and PE reconstruction with the change of breaking point. Asterisks represent the breaking point of ideal DE spectrum. Dotted line means the PSNR of ideal 7-bin.

We have measured PSNR for different cases including SwDE, realistic MECT and ideal MECT. For convenience, we only present 7 energy bins as MECT. Information about more energy bins for MECT can be seen in the next section. The results are summarized in Table 2. From Table 2, it can be seen that generally Bouman's weighting method works much better than that without weighting, especially for the phantom with high attenuation. Moreover, if we observe the table horizontally, in some cases where no weight is added, ideal energy bin

is better than the realistic one, which is modeled by E Roessl and C Herrmann.[17] However, the difference is almost identical between "real 7 bin" and "ideal 7 bin" if we use weighting. In particular, the ideal dual-energy bin works better than SwDE, which indicates the potential advantage of using photon counting detector for reconstruction since the spectra of MECT do not overlap as much as SwDE.

The results above assume that each energy bin is of equal width. Because there are different ways to divide the energy spectrum, we ploted the PSNR with respect to breakpoints for the case of two ideal energy bins (Fig. 5). It can also be observed that 7 energy bins always gives rise to better results compared to two bins. Moreover, the increase of the amount of metal in the phantom also considerably deteriorates the PSNR, especially when no weighting is applied.

In our results, the combination of weighting and multi-energy photon counting detector can noticeably improve the reconstruction compared with the traditional SwDE. For instance, by comparing Fig. 6 and 7, Fig. 8 and 9, Fig. 10 and 11, it demonstrates the obvious advantage of multi-energy photon counting detector for high, medium and low attenuation respectively. In particular, the artifacts in Fig. 6 are largely reduced, where large amount of metal appears in the phantom.

The sensitivity of multi-energy reconstruction to errors in modeling the detector sensitivity function (Eq.14) was also studied, in the extreme case where energy overlap was included in simulation but ignored in reconstruction. Two spectra were used to reconstruct the Compton and PE images for the simulation of multi-energy bins, abbreviated as "mismatch" and "match". Here "mismatch" means using ideally divided multi-bins spectrum (right one of Fig. 2) to reconstruct Compton and PE image and "match" means using realistic multi-bins spectrum (right one of Fig. 3) to reconstruct. In the comparison between "mismatch" and "match", a noticeable improvement can be seen for "match", which reconstruct Compton and PE image using realistic multi-bins spectrum. The result of "match" method is very close to the result of ideal 7-energy bin, especially using the Bouman's weighting method. It makes sense because the sinogram of each bin is built by the same realistic multi-energy spectrum. Therefore, it is better to use the exactly same spectrum to estimate Compton and PE coefficients than use the spectrum that does not match the original spectrum. Nonetheless, even with the "mismatch" spectrum, the results of MECT are still much better than SwDE.

4.2 Multi-energy bin using photon counting detector

Compared to the SwDE, the results have shown the advantage of multi-energy bin using photon counting detector. However, it is worth studying how many bins are needed to obtain a good result because the extra accuracy may entail a large amount of investment for the devices that can meet the requirement. In this case, the expense on a device increases with the incremental number of bins. Furthermore, it will be expensive to estimate Compton and PE coefficients if too many energy bins are used because of the increasing dimensionality. For instance, the time used for Compton and PE reconstructions of phantom with high attenuation in our experiment is 500 s, 543 s, 638 s, 687 s for SwDE, 2 bins realistic MECT, 7 bins realistic MECT, 20 bins realistic MECT, respectively. Thus there exists a tradeoff between a larger bin number and less computational time.

The results show that the increase of the number of bins can reduce the MSE especially when the bin number is less than 5 (Fig. 12). However, the MSE curves finally converge to a certain value. Because continuously increasing the number of bins cannot further improve the reconstructions, it is sensible to pick an appropriate bin number to make a trade-off between the cost of using multi-energy bin and the improvement it can bring.

Fig. 13 and Fig. 14 show that the metal has an influence on both metal region and non-metal region. This is because the appearance of metal leads to a large number of streaks across the reconstructed images. Thus, we separate the phantom into two parts. One is aluminum (Al) region. Another is non-Al region where the aluminum is eliminated from the phantom. Based on the results, the MSE of the Al region is much larger than the MSE of non-Al region. Therefore, the noise of the whole reconstructed image is mainly contributed by the Al region. The MSE of non-Al region also decreases when more energy bins are applied. This means that multi-energy bin method is effective to reduce the noise not only in the Al region, but also the non-Al region which is influenced by the artifacts produced by the aluminum. Furthermore, the amount of aluminum in the phantom makes a difference to the MSE. The MSE of medium attenuation is much lower than the one of higher attenuation, as we saw in section 4.1.

5. CONCLUSIONS

In this paper, we studied how the metal in the phantom exerts a negative influence on the Compton and PE reconstruction with performance degrading with the increasing amount of metal in the phantom. The use of multiple energy bins improves the PSNR compared to SwDE. We then use multi-energy detectors combined with a weighted least squares method to reconstruct Compton and PE images. Weighted MECT considerably improves the reconstruction results especially when a large amount of metal appears, which is potentially helpful for practical applications. We also explored the benefit of using more energy bins. Increasing the number of energy bins improves the reconstruction, though gains become minimal once roughly ten bins are reached. However, the ideal number of bins will be scenario-dependent.

Our future work will focus on the further improvement of Compton and PE reconstructions. Furthermore, reconstruction from actual experimental data will be an important part of future work.

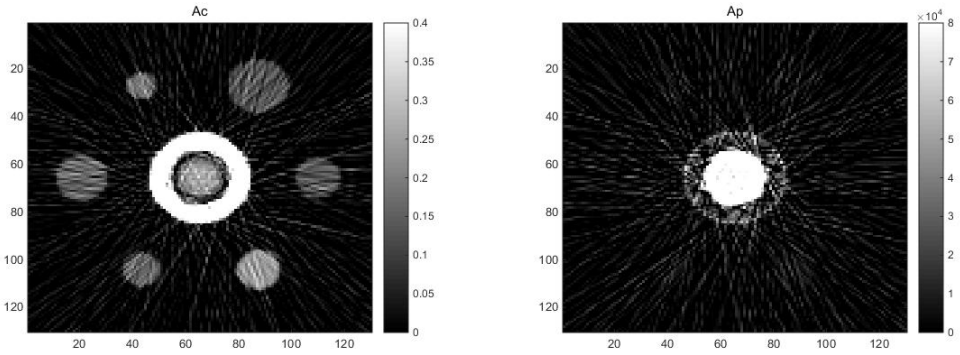

Figure 6. These two plots shows the reconstruction using SwDE approach for the high attenuation phantom. Left column is Compton image and right column is photoelectric image. Following figures have the same arrangement.

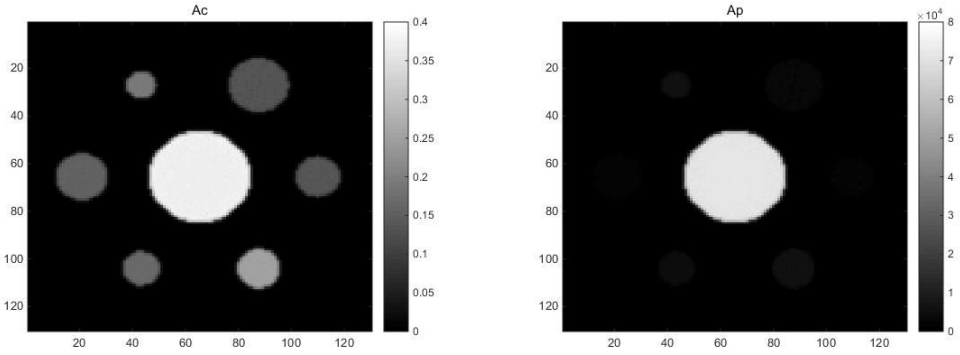

Figure 7. The plots show the reconstruction using realistic 7-energy bins with weighting for high attenuation phantom.

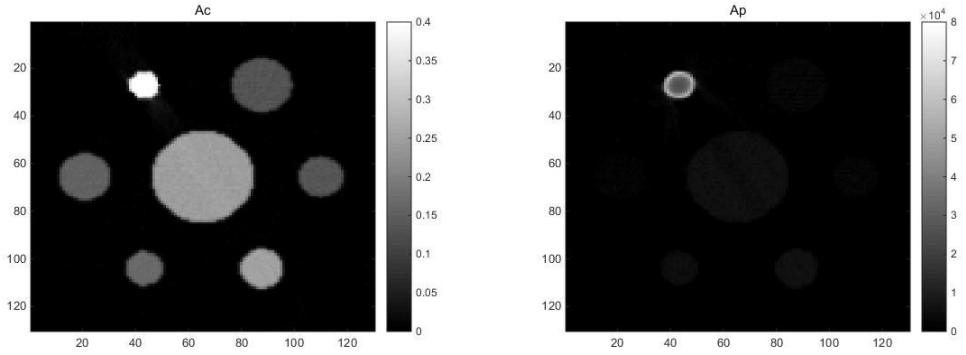

Figure 8. The plots shows the reconstruction using SwDE approach for the medium attenuation phantom.

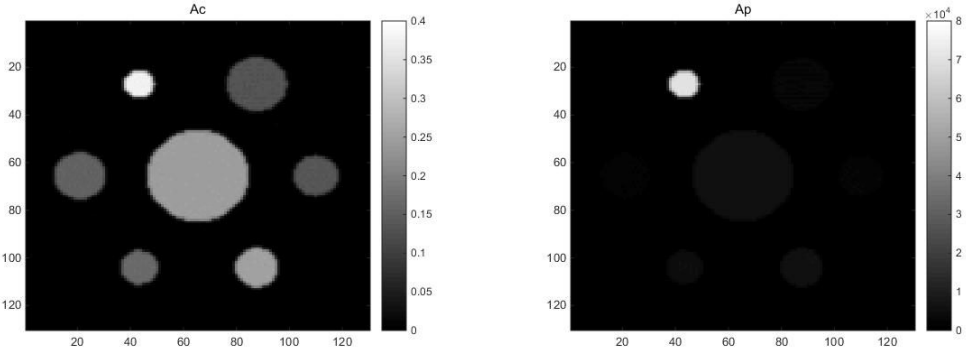

Figure 9. The plots shows the reconstruction using realistic 7-energy bins with weighting for high attenuation phantom.

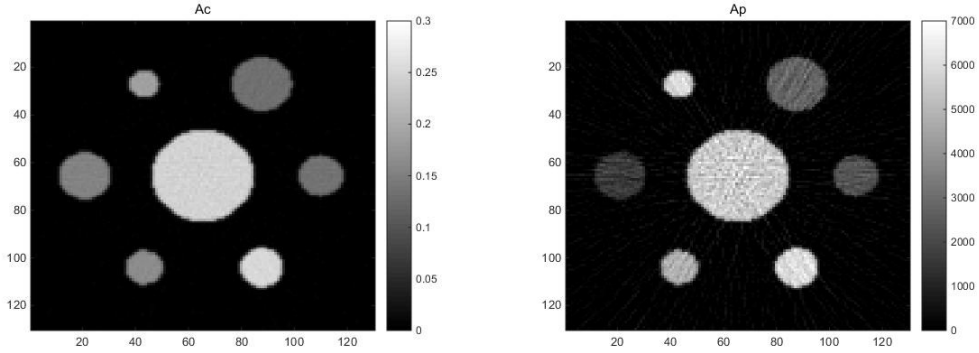

Figure 10. The plots shows the reconstruction using SwDE approach for the low attenuation phantom.

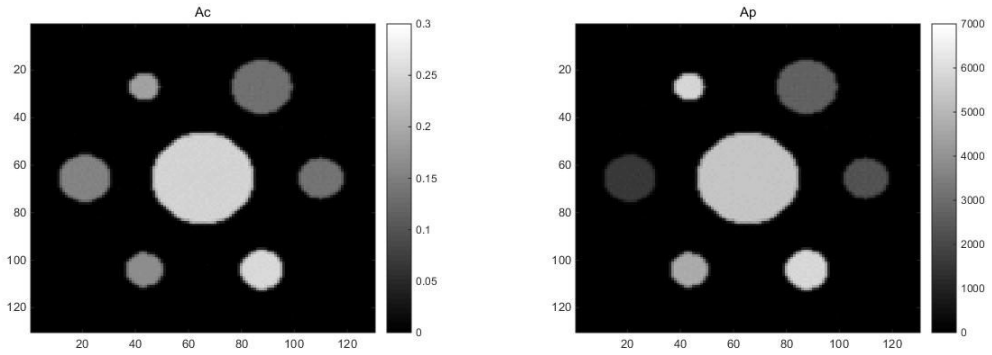

Figure 11. The plots shows the reconstruction using realistic 7-energy bins with weighting for low attenuation phantom.

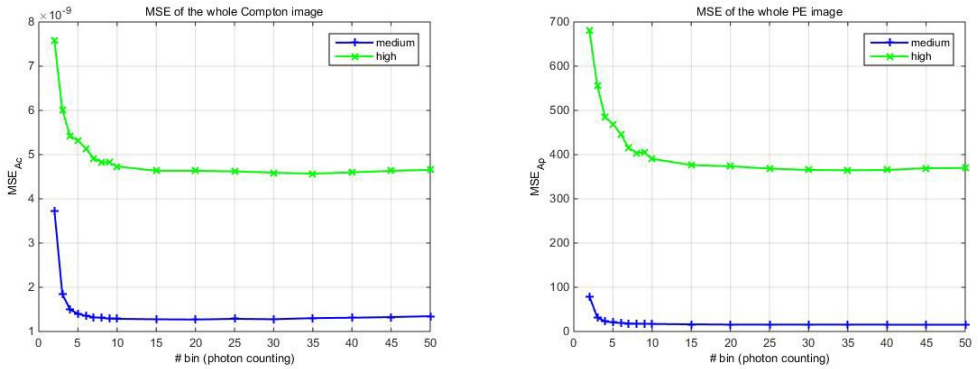

Figure 12. The plots show that for the whole phantom, MSE decreases with the increment of the number of bins, showing the benefit of using more energy bins. Left column is MSE for Compton image and right column is MSE for PE image. Each data shown is the average of 30 random simulations.

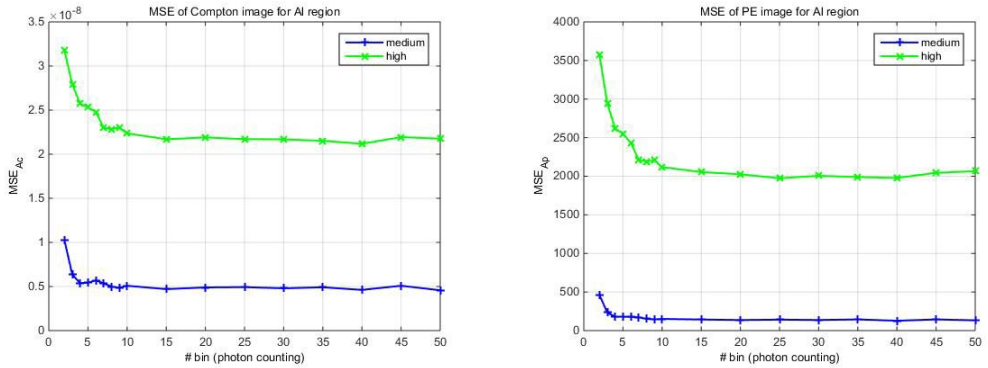

Figure 13. The plots show the decrease of MSE of aluminum region for both Compton and PE images. The rate of the decrease of MSE also diminishes when the number of bins increases.

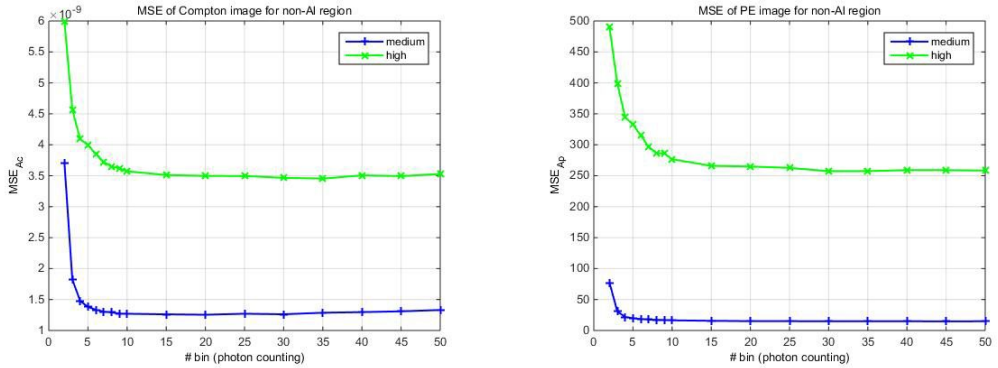

Figure 14. The plots also show the decrease of MSE of non-aluminum region for both Compton and PE images. These plots demonstrate that the multi-energy bin can also reduce the noise in the region where no aluminum appears.

ACKNOWLEDGMENTS

This material is based upon work supported by the U.S. Department of Homeland Security, Science and Technology Directorate, Office of University Programs, under Grant Award 2013-ST-061-ED0001. The views and conclusions contained in this document are those of the authors and should not be interpreted as necessarily representing the official policies, either expressed or implied, of the U.S. Department of Homeland Security.

REFERENCES

[1] Singh, S. and Singh, M., "Explosives detection systems (eds) for aviation security," *Signal Processing* **83**(1), 31–55 (2003).

[2] Fainberg, A., "Explosives detection for aviation security," *Science* **255**(5051), 1531 (1992).

[3] McCullough, E. C., "Photon attenuation in computed tomography," *Medical Physics* **2**(6), 307–320 (1975).

[4] Eilbert, R. F. and Krug, K. D., "Aspects of image recognition in vivid technologies' dual-energy x-ray system for explosives detection," in [*Applications in Optical Science and Engineering*], 127–143, International Society for Optics and Photonics (1993).

[5] Alvarez, R. E. and Macovski, A., "Energy-selective reconstructions in x-ray computerised tomography," *Physics in medicine and biology* **21**(5), 733 (1976).

[6] Ying, Z., Naidu, R., and Crawford, C. R., "Dual energy computed tomography for explosive detection," *Journal of X-ray Science and Technology* **14**(4), 235–256 (2006).

[7] Watzke, O. and Kalender, W. A., "A pragmatic approach to metal artifact reduction in ct: merging of metal artifact reduced images," *European radiology* **14**(5), 849–856 (2004).

[8] Boas, F. E. and Fleischmann, D., "Ct artifacts: causes and reduction techniques," *Imaging in Medicine* **4**(2), 229–240 (2012).

[9] La Rivière, P. J., Bian, J., and Vargas, P. A., "Penalized-likelihood sinogram restoration for computed tomography," *Medical Imaging, IEEE Transactions on* **25**(8), 1022–1036 (2006).

[10] Gorecki, A., Brambilla, A., Moulin, V., Gaborieau, E., Radisson, P., and Verger, L., "Comparing performances of a cdte x-ray spectroscopic detector and an x-ray dual-energy sandwich detector," *Journal of Instrumentation* **8**(11), P11011 (2013).

[11] Semerci, O. and Miller, E. L., "A parametric level-set approach to simultaneous object identification and background reconstruction for dual-energy computed tomography," *Image Processing, IEEE Transactions on* **21**(5), 2719–2734 (2012).

[12] Sauer, K. and Bouman, C., "A local update strategy for iterative reconstruction from projections," *Signal Processing, IEEE Transactions on* **41**(2), 534–548 (1993).

[13] Bouman, C. A. and Sauer, K., "A unified approach to statistical tomography using coordinate descent optimization," *Image Processing, IEEE Transactions on* **5**(3), 480–492 (1996).

[14] Thibault, J.-B., Bouman, C. A., Sauer, K. D., and Hsieh, J., "A recursive filter for noise reduction in statistical iterative tomographic imaging," in [*Electronic Imaging 2006*], 60650X–60650X, International Society for Optics and Photonics (2006).

[15] Semerci, O., Hao, N., Kilmer, M. E., and Miller, E. L., "Tensor-based formulation and nuclear norm regularization for multienergy computed tomography," *Image Processing, IEEE Transactions on* **23**(4), 1678–1693 (2014).

[16] Iwanczyk, J. S., Nygård, E., Meirav, O., Arenson, J., Barber, W. C., Hartsough, N. E., Malakhov, N., and Wessel, J. C., "Photon counting energy dispersive detector arrays for x-ray imaging," *Nuclear Science, IEEE Transactions on* **56**(3), 535–542 (2009).

[17] Roessl, E. and Herrmann, C., "Cramér–rao lower bound of basis image noise in multiple-energy x-ray imaging," *Physics in medicine and biology* **54**(5), 1307 (2009).